Hierarchical SnO$_2$ hollow nanotubes as anodes for high performance lithium-ion battery

Yang Liu[1], Peng Zhang[1,2,*] , Yuxiong Xue[1], Min Zhou[1], Rongxing Cao[1], Penghui Chen[1], and Xianghua Zeng[1]

[1] College of Electrical, Energy and Power Engineering, Yangzhou University, Yangzhou 225000, China
[2] School of Material Science and Engineering, Harbin University of Science and Technology, Harbin 150000, China

ABSTRACT

Nanostructured transition metal oxides are promising anode materials for lithium-ion batteries. Nevertheless, the problem of high volume expansion rate limits its further application. In this paper, we present a 3D hierarchical SnO$_2$ hollow nanotubes material by calcining C@SnS$_2$ materials in the air. This structure combines the advantages of both the hollow nanotubes and the outer staggered nanosheets structure, in which the hollow nanotube can provide more lithium ion transport channels, the space between the tubes can buffer the volume change, and the staggering nanosheets structure can effectively improve the relative specific surface area of the material and improve the storage capacity. As a result, the SnO$_2$ hollow nanotubes anode exhibits the highly reversible capacity of 1079 mAh g^{-1} at a current density of 100 mA g^{-1}, while the reversible specific capacity of 770 mAh g^{-1} was obtained after 100 cycles. The research results obtained in this work provide a feasible strategy for synthetic nanoscale transition metal oxide as high-performance lithium anode material.

1 Introduction

Nowadays, with the rapid development of advanced technology, more and more lithium-ion battery products are widely used in everyday life (smartphones, cameras, automobiles, computers, and so on). The best future promising for energy storage devices will be lithium-ion batteries with higher energy density, longer working life, and excellent cycling stability. However, the development of lithium-ion batteries has been restricted because it is a lower theoretical capacity (372 mAh g^{-1}) of graphite anode. As an anode material, transition metal oxide usually has a relatively high theoretical storage capacity [1]. Common transition metal oxides (M$_x$O$_y$) include Mn [2], Fe [3], Sn [4], Ni [5], Cu [6], Co [7], etc.

Because of its low potential of lithium-ion de-intercalation, the high theoretical storage capacity of lithium-ion (781 mAh g^{-1}), abundant natural resources, environmentally friendly and convenient preparation, SnO$_2$ has been considered as an ideal anode material in transition metal oxide [8].

Nevertheless, as SnO_2 material produces large volume expansion during the lithium-ion de-intercalation process, resulting in the attenuation of storage capacity. The chief cause of the current phenomenon is the phase transition during the reaction process. The effect is exacerbated by the concentration difference in the direction of lithium ion diffusion [9]. The decreasing of storage capacity and rate performance is caused by the slow diffusion of lithium ions in the phase. The concentration difference of lithium-ion diffusion can result in stress concentration and aggravate volume change.

In order to conquer these defects, the usual method to improve it is to prepare new nano-structured [10–12]. Nanostructured material has a high specific surface area advantage over other materials and has effectively increased storage capacity. Double-shelled nanostructure of SnO_2@C tube shows an outstanding electrochemical performance that 462.5 mAh g^{-1} are retained at 1 A g^{-1} after 450 cycles [13]. SnO_2/TiO_2@CNFs carbon nanofibers exhibit a remarkable specific capacity of 766.1 mAh g^{-1} after 200 cycles. The flexible and conductive carbon nanofiber matrix accommodates volume changes and increases overall electronic conductivity [14]. While nanostructured material can substantially improve storage capacity, it is not good structural stability. The cyclic stability of nanomaterials can be effectively improved by reasonably designing the hollow structure. Porous SnO_2/graphene composite thin films exhibit capacity retention of 551.0 mAh g^{-1} after the 100th cycle at 200 mA g^{-1} [15]. Porous SnO_2 hollow microspheres as anodes deliver a capacity of 602 mAh g^{-1} after the 100th cycle at 200 mA g^{-1} [16]. Therefore, the electrochemical properties of SnO_2 materials can be greatly improved through the rational design of hierarchical hollow nanomaterials.

This paper designs a new type of LIBs anode materials of hierarchical SnO_2 hollow nanotubes. This structure combines the advantages of both the hollow nanotubes and the outer staggered nanosheets structure. The hierarchical structure has a higher relative specific surface area. It provides more active sites for redox reaction and improves the storage capacity of lithium ions. At the same time, the hollow tube structure can effectively lithium-ion transport performance and buffer the volume change during the charging and discharging process. As a result, this electrode material exhibits enhanced specific capacity, as well as favorable rate capability and cycling stability.

2 Experimental section

2.1 Materials and characterization equipment

Polyvinylpyrrolidone (PVP; Mw 1,300,000 g mol^{-1}) and dimethylformamide (DMF, ≥ 99 %) were purchased from Aladdin Co. Ltd. Stannic chloride pentahydrate ($SnCl_4 \cdot 5H_2O$, ≥ 99 %) and thioacetamide (TAA) were provided by China National Pharmaceutical Industry Co. Ltd. All the chemicals and materials were used without further purification.

The microstructure and morphology of the samples were observed by SEM (Apreo). The crystal microstructures of the samples were characterized by powder XRD on PANalytical X'Pert (Cu-Kα radiation; λ = 1.54178 Å). The electrochemical test was carried out by the electrochemical workstation of the Shanghai Chenhua Company (CHI600E), and the lithium battery test was carried out by a blue battery test system (CT3001A).

2.2 Material preparation

2.2.1 Synthesis of carbon nanofibers

In a typical procedure, an electrospinning solution containing PVP (3.5 g) and DMF (20 mL) was dissolved with vigorous magnetic stirring for over 6 h at ambient temperature. During the spinning process, a DC voltage of 15 kV was applied to form a high potential difference, and the flow rates were controlled at 0.6 mL h^{-1}. The distance between the needle tip and the grounded aluminum sheet was 15 cm. Afterward, the spun fibers were torn off using tweezers and placed as a thin layer on a clear glass slice. Finally, the spun fibers were cured at 300 °C for 1 h in a tubular furnace at a heating rate of 5 °C min^{-1}. Besides, the fibers were annealed at 600 °C for 1.5 h in a tubular furnace with a heating rate of 5 °C min^{-1} under Ar/H_2 atmosphere in the whole process and cooled naturally at room temperature.

2.2.2 Fabrication of C@SnS$_2$ nanotubes

SnCl$_4$·5H$_2$O (0.35 g) and TAA (0.8 g) were dissolved in ethanol (80 mL) with vigorous magnetic stirring. The prepared carbon fibers were cut into a size of 2 × 5 cm with mixed solution added and then transferred into a 100 mL Teflon-lined autoclave. Then heated at 160 °C for 12 h. After cooling down naturally, the obtained C@SnS$_2$ samples were washed with deionized water and alcohol for three times respectively. Finally, the C@SnS$_2$ nanotubes were obtained via drying at 60 °C for 6 h in a vacuum oven.

2.2.3 Fabrication of hierarchical SnO$_2$ hollow nanotubes

The C@SnS$_2$ nanotubes were calcinated at 600 °C for 2 h in a tubular furnace with a heating rate of 2 °C min^{-1} in the air atmosphere. The hierarchical SnO$_2$ hollow nanotubes were fabricated.

2.2.4 Fabrication of SnO$_2$ nanoparticles

SnCl$_4$·5H$_2$O (0.35 g) and TAA (0.8 g) were dissolved in ethanol (80 mL) with vigorous magnetic stirring. Then transferred into a 100 mL Teflon-lined autoclave, and later heated at 160 °C for 12 h. After cooling down naturally, the obtained nanosheets cluster SnS$_2$ obtained C@SnS$_2$ samples were washed with deionized water and alcohol for three times respectively. The nanosheets cluster SnS$_2$ were calcinated at 600 °C for 2 h in a tubular furnace with a heating rate of 2 °C min^{-1} in the air atmosphere. SnO$_2$ nanoparticles were fabricated.

2.3 Electrochemical measurement

The samples (SnO$_2$ hollow nanotubes, C@SnS$_2$ nanotubes, and SnO$_2$ nanoparticles), the conductor (acetylene black), and the binder (PVDF) were ground uniformly at a ratio of 8:1:1. The mixed material was dripped with NMP (N-methyl pyrrolidone) solution and evenly applied to the copper foil collector. It was dried at 60 °C for 12 h and cut into a 12 mm diameter wafer as the cathode electrode. The mass loading of active materials was approximately 1.2 mg per wafer. The other key materials of the battery were pure lithium sheets with a diameter of 12 mm serving as the electrode and 20 mm PE (Celgard 2400) serving as the diaphragm. 1 M LiPF$_6$ was used as the electrolyte in the mixed solution of vinyl carbonate (EC), Methyl carbonate (EMC), and dimethyl carbonate (DMC) (V:V:V = 1:1:1). The half button cells (CR2032) were assembled in a glove box (H$_2$O/O$_2$ < 0.1 PPM).

Galvanostatic curves, cycling performances, and rate performances were carried out in the potential range of 0.01–3.0 V at different current densities of 0.1 to 2 A g^{-1}. The measurements of cyclic voltammetry (CV, 0.01–3.0 V with a scan rate of 0.1–1 mV s^{-1}) and electrochemical impedance spectroscopy (EIS, 100 k-0.01 Hz with an amplitude of 5 mV) were performed on an electrochemical workstation.

3 Results and discussion

The synthetic process of hierarchical SnO$_2$ hollow nanotubes is shown in scheme 1. Firstly, the carbon nanofibers have been obtained by electrostatic spinning with PVP and DMF. Subsequently, the as-treated carbon nanofibers are used as substrate material for the growth of SnS$_2$ sheets by the hydrothermal method with thioacetamide TAA as the S source and SnCl$_4$·5H$_2$O as the Sn source. Finally, the carbon fibers inside the C@SnS$_2$ composite material disappear in high-temperature oxidation, and the SnS$_2$ sheets material is oxidized to form hierarchical SnO$_2$ hollow nanotubes. SnO$_2$ nanoparticles samples are synthesized by hydrothermal method and high-temperature oxidation for comparison of SnO$_2$ hollow nanotubes.

Firstly, the microstructure of different samples was observed by a scanning electron microscope (Fig. 1). Figure 1a, b clearly show the structural morphology of carbon nanofibers prepared by electrostatic spinning. By observing the SEM picture of carbon nanofibers, it was found that carbon nanofibers are about 190 nm in diameter uniform and exquisite. This fiber is 40 times less than the diameter of carbon cloth [17, 18]. Electrospinning carbon nanofibers can provide more growth locations in the same area. The carbon nanofibers are densely crossed and arranged with interstitial space, which provides a suitable substrate for SnS$_2$ nanosheets to grow. The microstructure of the C@SnS$_2$ can be seen that the original carbon nanofibers surface is densely covered with SnS$_2$ nanosheets from Fig. 1c, d. C@SnS$_2$ composite material has a uniform linear thickness and reasonable clearance. It is about 390 nm in diameter.
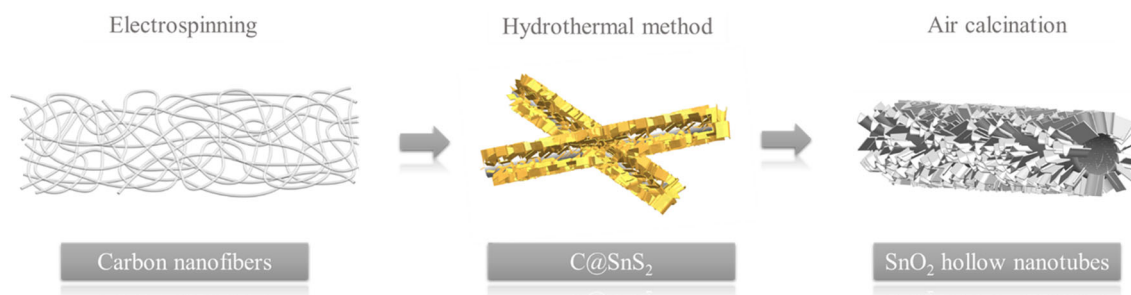
Scheme 1 Schematic illustration of the synthetic process for SnO$_2$ hollow nanotubes
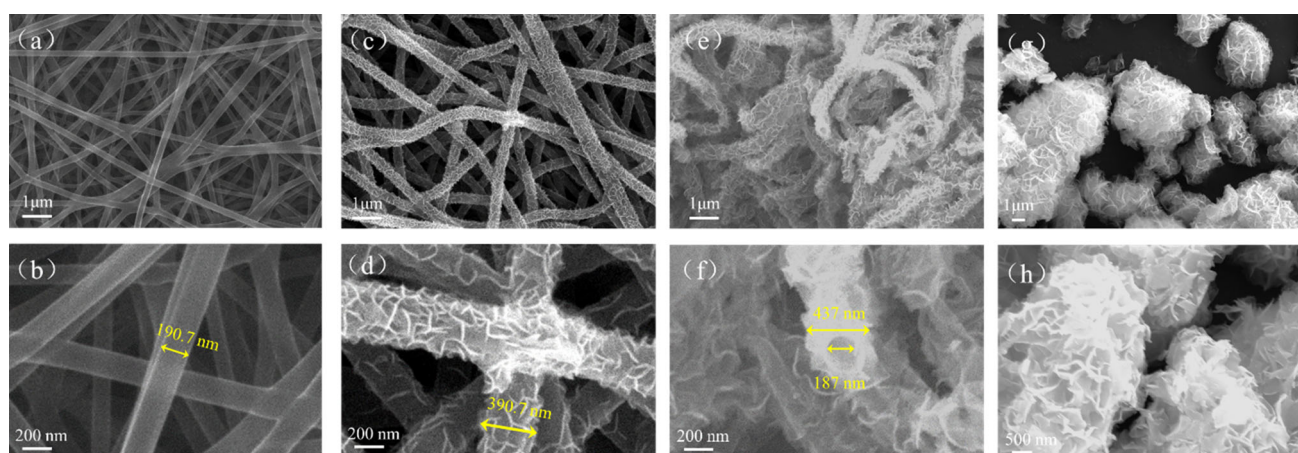
Fig. 1 Scanning electron microscope (SEM) morphologies of different samples **a**, **b** carbon nanofibers; **c**, **d** C@SnS$_2$ nanotubes; **e**, **f** SnO$_2$ hollow nanotubes; **g**, **h** SnO$_2$ nanoparticles

Figure 1e, f show the microstructure of hierarchical SnO$_2$ hollow nanotubes. Its hollow structure has an inside diameter of 187 nm and an outside diameter of 437 nm. After oxidation, its shape remains unchanged and the texture becomes robust, which will play a better supporting role during the cycle test. At the same time, increasing relative specific surface area will provide more lithium-ion attachment sites. SnO$_2$ nanoparticle material is composed of abundant stacked nanosheets structure from Fig. 1g, h. According to the EDS spectrum of the SnO$_2$ hollow nanotubes in Fig. 2, it can be seen that the SnO$_2$ sample mainly consists of Sn and O elements, while C and S elements remain very little. This proves that C@SnS$_2$ is completely reacted in the process of high temperature conversion.

Crystal structure and phase composition of hierarchical SnO$_2$ hollow nanotubes are characterized by the XRD test (Fig. 3). The main diffraction peaks can exactly match the SnO$_2$ standard JCPDS card (No. 41-1445). The main peaks 26.6°, 33.89°, and 51.78°

correspond to (110), (101), and (211) respectively. There are no impurities peaks in the XRD patterns. This would indicate that the hierarchical SnO$_2$ hollow nanotubes have purified SnO$_2$ crystal material composition.

According to the above characterization, it is seen that SnO$_2$ materials with hierarchical hollow nanotubes structures which have been successfully prepared possess evident advantages over the common SnO$_2$ nanomaterials including larger interface area, abundant hollow channel spaces, and highly hierarchical robust structure.

Half-cells assembled with different samples are used for electrochemical performance testing (Fig. 4). The CV curves of SnO$_2$ hollow nanotubes tested are shown in Fig. 4a. The reaction mechanism of SnO$_2$ has two chemical reactions during charging and discharging (Eqs. 1 and 2) [19, 20]. Equation 11 is dominated by the forward reaction. SnO$_2$ is transformed into Sn metal and Li$_2$O, which is reflected by a reduction peak of about 1 V in the CV curve [15]. The SnO$_2$ nanostructured will make reaction 1
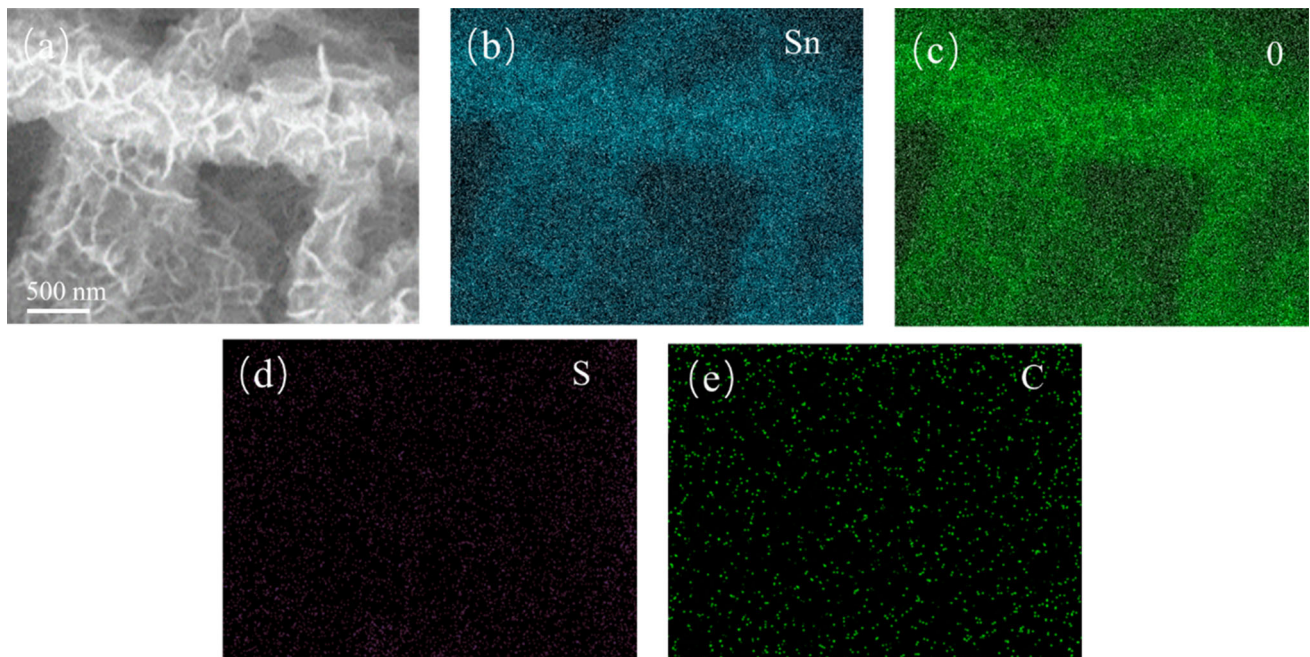
Fig. 2 EDS mapping (Sn, S, C and O elements) of the SnO$_2$ hollow nanotubes
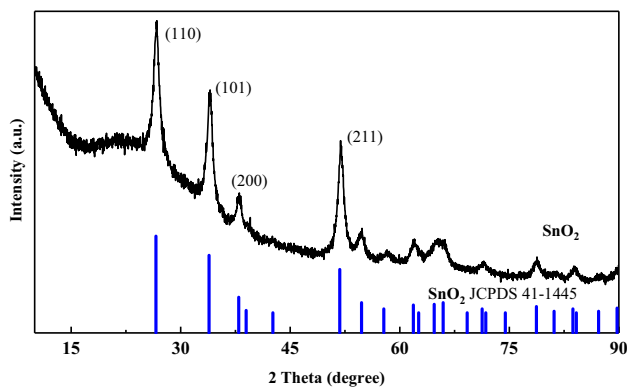
Fig. 3 XRD patterns of SnO$_2$ hollow nanotubes

partially reversible. A small amount of Sn is transformed into SnO and SnO$_2$ (weak oxidation peak around 1.25–1.7 V) [21]. It causing the test capacity to exceed the theoretical specific capacity and improving cycling stability. The second step is that the metal Sn reacts reversibly with the lithium-ion to form Li$_x$Sn (Eq. 2). Reduction peaks near 0.3 and 0.55 V represent the lithium intercalation process in which Sn and Li$^+$ are alloyed to form Li$_x$Sn [21–23]. The oxidation peak near 0.5 V represents the de-intercalation process of Li$_x$Sn alloy. When x is 4.4 in Li$_x$Sn, the theoretical capacity reaches a maximum of 781 mAh g^{-1} [24, 25]. In the comparison between the first cycle and subsequent cycles of the CV curve, it is

observed that some peaks reduce (reduction peak around 1 and 0.3 V) and disappear (oxidation peak around 0.6 V), which is due to the formation of SEI (Solid Electrolyte Interphase) films in the first cycle (Li$^+$ + e$^-$ + electrolyte → SEI (Li)). The initial irreversible capacity loss is related to the inevitable formation of a solid electrolyte interface (SEI) film. The reaction process of the material can also be reflected by the specific capacity-voltage curves of the first five turns of different samples in Fig. 4c–e.
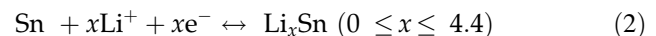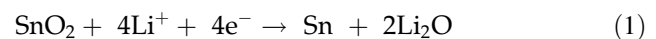
$$SnO_2 + 4Li^+ + 4e^- \rightarrow Sn + 2Li_2O \qquad (1)$$

$$Sn + xLi^+ + xe^- \leftrightarrow Li_xSn \ (0 \leq x \leq 4.4) \qquad (2)$$

Figure 4b shows the rate performance of SnO$_2$ hollow nanotubes, SnO$_2$ nanoparticles, and C@SnS$_2$ samples with different current densities (at 0.1–2 A g^{-1}). The rate performance of SnO$_2$ hollow nanotubes is optimal as a whole, with a specific capacity of about 1024 mAh g^{-1} at 0.1 A g^{-1}. SnO$_2$ nanoparticles have the worst rate performance, with a specific capacity of about 25 mAh g^{-1} at a high current density of 2 A g^{-1}. The circulation capacity loss in the early stage is mainly caused by the formation of a solid electrolyte interface (SEI). The excellent rate performance of SnO$_2$ hollow nanotubes is mainly due to the hierarchy. The hollow tubular structure, as a lithium-ion transport channel, can effectively improve transport efficiency and alleviate volume
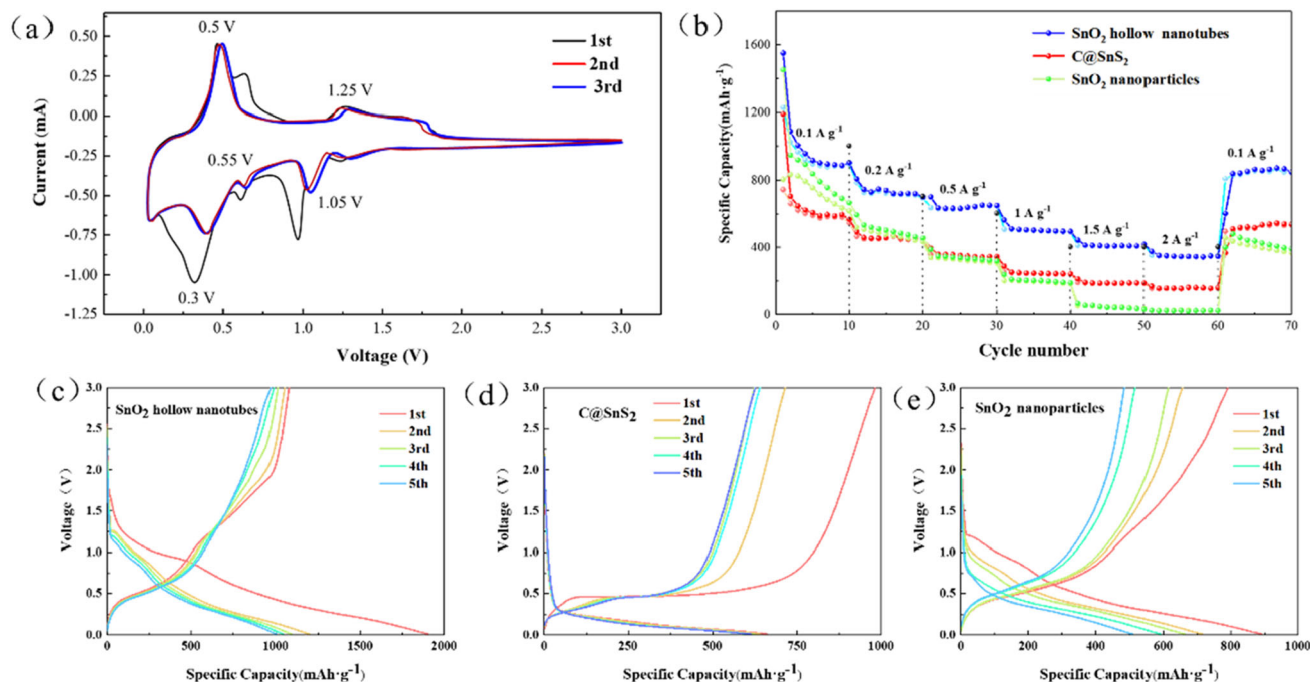
Fig. 4 Electrochemical performance of C@SnS$_2$ nanotubes, SnO$_2$ nanoparticles, and SnO$_2$ hollow nanotubes: **a** CV curves of SnO$_2$ hollow nanotubes at a scan rate of 0.1 mV s^{-1}; **b** rate performance of samples; **c**, **d**, **e** specific capacity-voltage profiles of samples at 0.1 A g^{-1}

expansion. The poor rate performance of C@SnS$_2$ is mainly due to the structural damage caused by excessive material volume change during charging and discharging. Although SnO$_2$ nanoparticles have a higher relative specific surface area, it has not support structure and corresponding transmission channel, which delays the movement of lithium ions, resulting in a fast attenuation of specific capacity and difficult recovery.

The cyclic performance test results of C@SnS$_2$ nanotubes, SnO$_2$ nanoparticles, and SnO$_2$ hollow nanotubes samples are shown in Fig. 5. The specific capacity of SnO$_2$ hollow nanotubes is around 1079 mAh g^{-1} (an initial coulombic efficiency of 56.7 %), and the specific capacity still reaches 770 mAh g^{-1} after 100 cycles (the capacity retention rate of 77 %). The cycling stability of SnO$_2$ hollow nanotubes is also relatively good under high current density (Fig. 5b). The initial specific capacity is about 473 mAh g^{-1}, and the specific capacity remains around 283 mAh g^{-1} after 200 cycles (the capacity retention rate of 64.1 %). The initial specific capacity of C@SnS$_2$ is about 660 mAh g^{-1} at 0.1 A g^{-1}, and the specific capacity remains around 280 mAh g^{-1} after 100 cycles (the capacity retention rate of 42.4 %), and the specific capacity is about 72 mAh g^{-1} after 200 cycles

at 2 A g^{-1}. The cyclic stability of SnO$_2$ nanoparticles is the worst, with the specific capacity remains around 210 mAh g^{-1} after 100 cycles at 0.1 A g^{-1} and 25 mAh g^{-1} after 200 cycles at 2 A g^{-1}.

The excellent cycling stability of SnO$_2$ materials is attributed to the hierarchical SnO$_2$ hollow nanotubes, which improve the contact relative specific surface area and effectively reduces the volume variation of materials during charging and discharging. Some relevant studies show that the volume expansion rate of SnO$_2$ and SnS$_2$ exceeds 200 % [26–28]. The hollow tubular structure not only relieves the pressure of volume expansion but also effectively improves the efficiency of lithium-ion transport. The surface of C@SnS$_2$ material is densely crisscrossed with nanosheets. When the volume changes too much, SnS$_2$ is easy to fall off the carbon nanofibers, resulting in capacity attenuation. SnO$_2$ nanoparticle material nanosheets are closely distributed and have no support structure. Although the initial specific capacity is high, the capacity attenuation is extremely serious, resulting in the worst performance of cyclic stability. The material of the hierarchical SnO$_2$ hollow nanotubes greatly improves its electrochemical performance and measured against previous studies (Table 1).

Fig. 5 Electrochemical performance of C@SnS$_2$ nanotubes, SnO$_2$ nanoparticles, and SnO$_2$ hollow nanotubes. **a** Cyclic stability of at 0.1 A g^{-1}; **b** cyclic stability of at 2 A g^{-1}
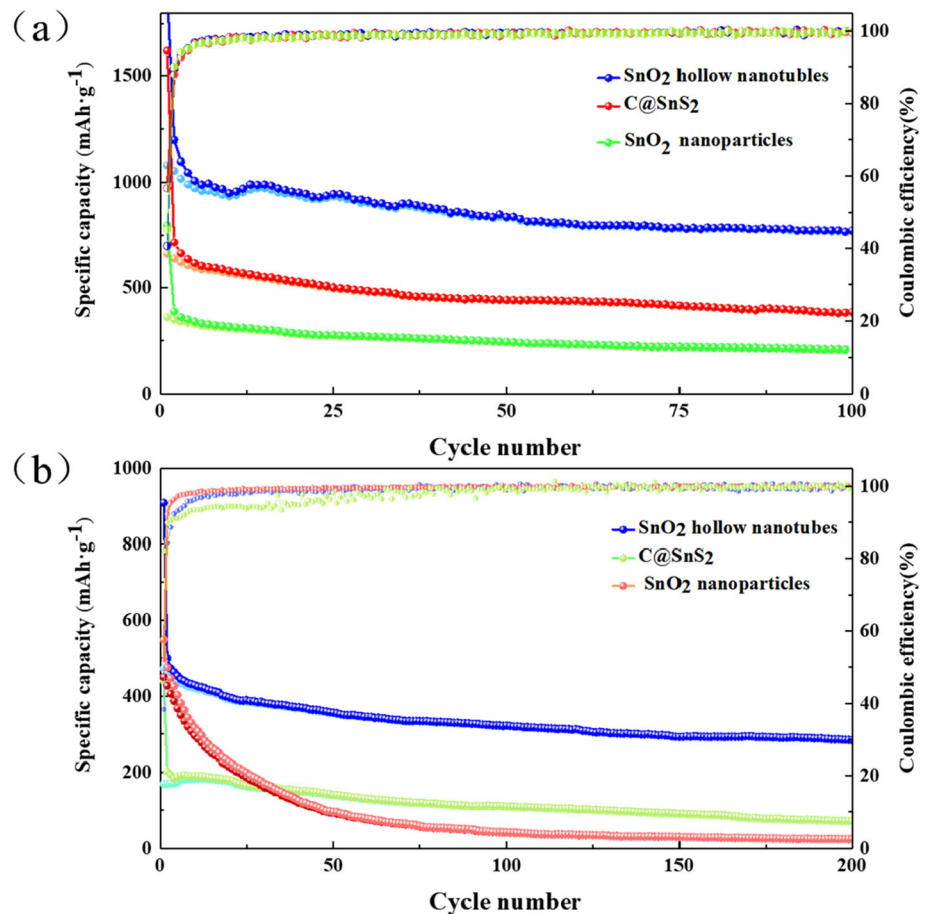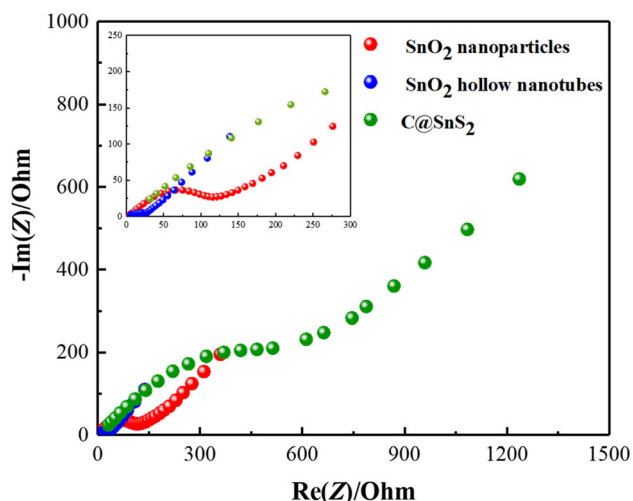

Then the EIS Nyquist plots of C@SnS$_2$ nanotubes, SnO$_2$ nanoparticles, and SnO$_2$ hollow nanotubes were tested (Fig. 6). The curves are composed of half-circle arcs in the low-frequency region and 45° oblique lines in the high-frequency region as a whole, which is related to charge transfer resistance (R_{ct}) and solid state diffusion (Z_w) of lithium-ion, respectively [35].

The charge transfer resistance (R_{ct}) of the SnO$_2$ hollow nanotubes (25 Ω) is the smallest, indicating a faster electron transfer process during the reaction. The large resistance (R_{ct}) of SnO$_2$ nanoparticles is caused by their loose structure. C@SnS$_2$ nanotubes sample has the highest resistance. The smaller semicircle diameter of the SnO$_2$ electrode can be indicated that the hierarchical hollow nanotubes structure is

Table. 1 Recent studies on electrochemical properties of SnO$_2$ lithium-ion batteries

Materials	First cycle specific capacity	Specific capacity after cycle	Retention ratio (%)
SnO$_2$ (in this paper)	1079 mAh g^{-1} at 0.1 A g^{-1}	770.8 mAh g^{-1} (100 cycles)	77
Porous SnO$_2$ [16]	≈ 900 mAh g^{-1} at 0.2 mA g^{-1}	504 mAh g^{-1} (100 cycles)	56
Graphene SnO$_2$ [29]	≈ 700 mAh g^{-1} at 0.2 A g^{-1}	695 mAh g^{-1} (500 cycles)	99
SnO$_2$@C/EG [30]	≈ 850 mAh g^{-1} at 0.2 A g^{-1}	662 mAh g^{-1} (100 cycles)	77
P-SnO$_2$@G [31]	≈ 915 mAh g^{-1} at 0.5 A g^{-1}	860 mAh g^{-1} (50 cycles)	94
SnO$_2$@C@GN [32]	≈ 1700 mAh g^{-1} at 0.2 A g^{-1}	882 mAh g^{-1} (70 cycles)	52
SnO$_2$@C DHNWs [13]	849.7 mAh g^{-1} at 1 A g^{-1}	462.5mAh g^{-1} (1000 cycles)	54.43
SnO$_2$@C nanosheet [33]	≈ 1000 mAh g^{-1} at 0.2 A g^{-1}	821mAh g^{-1} (100 cycles)	54.43
SnO$_2$ NRS/G [34]	723 mAh g^{-1} at 20 mA g^{-1}	About 200 mAh g^{-1} (80 cycle)	27.7

Fig. 6 EIS Nyquist plots of C@SnS$_2$ nanotubes, SnO$_2$ nanoparticles, and SnO$_2$ hollow nanotubes

conductive to rapid charge transfer, thus providing better electrochemical performance for LIBs.

In conclusion, the excellent electrochemical performance of SnO$_2$ structural materials is influenced by the following factors. The synthesized SnO$_2$ material is a kind of hollow nanotubes structure with interlaced sheets stacked. This structure combines the advantages of both the hollow nanotube and the outer staggered nanosheets structure. This nanotube structure has a rich and reasonable void space structure, which can effectively shorten the lithium-ion transport path and extend the rate performance. This kind of interlaced sheets stacked hollow structure has a higher relative specific surface area, which can effectively provide more attachment sites for the lithium-ion de-intercalation, thus improving the specific capacity of the material. At the same time, the hierarchical SnO$_2$ hollow nanotube structure has reasonable space for buffer volume change, which effectively improves the cycle stability of the anode material.

4 Conclusions

In summary, interlaced sheets stacked SnO$_2$ hollow nanotubes were successfully fabricated by air calcining C@SnS$_2$ materials. Due to the unique hollow nanotube nanostructure, the nanocomposite displays excellent electrochemical performance as an anode material in lithium-ion batteries. The SnO$_2$ hollow nanotubes anode exhibits the highly reversible

capacity of 1079 mAh g^{-1} with an initial coulombic efficiency of 56.7 % at a current density of 100 mA g^{-1}, while the reversible specific capacity of 770 mAh g^{-1} was obtained after 100 cycles. This unique SnO$_2$ material provided in this work manifested a synthesis method of transition metal oxide nanomaterials to promote the performance of lithium electrodes.

Declarations

Conflict of interest On behalf of all authors, the corresponding author states that there is no conflict of interest.

References

1. Z. Xiao, R. Wang, D. Jiang, Z. Qian, Y. Li, K. Yang, Y. Sun, Z. Zeng, F. Wu, ACS Appl. Energy Mater. (2021). https://doi.org/10.1021/acsaem.1c01259
2. B Jia, W Chen, J Luo, Z Yang, L Li, L Guo, Adv. Mater. **32**, 1906582 (2019)
3. KO Ogunniran, G Murugadoss, R Thangamuthu, ST Nishanthi, J. Alloy. Compd. **786**, 873 (2019)
4. J Liang, L Zhang, D XiLi, J Kang, Electrochim. Acta **341**, 136030 (2020)
5. W Zhang, P Cao, L Li, K Yang, K Wang, S Liu, Z Yu, Chem. Eng. J. **348**, 599 (2018)
6. B Wang, X-L Wu, C-Y Shu, Y-G Guo, C-R Wang, J. Mater. Chem. **20**, 10661 (2010)
7. C Guo, W Zhang, Y Liu, J He, S Yang, M Liu, Q Wang, Z Guo, Adv. Funct. Mater. **29**, 1901925 (2019)
8. S Gao, N Wang, S Li, D Li, Z Cui, G Yue, J Liu, X Zhao, L Jiang, Y Zhao, Angew. Chem. Int. Ed. Engl. **59**, 2465 (2020)
9. JS Chen, LC Yan, TC Yuan, N Jayaprakash, S Madhavi, HY Yan, WL Xiong, J. Phys. Chem. C **113**, 20504 (2009)
10. Y Chen, QZ Huang, J Wang, Q Wang, JM Xue, J. Mater. Chem. **21**, 17448 (2011)
11. F Li, G Luo, J Yu, W Huang, D Xu, W Chen, X Huang, S Yang, Y Fang, X Yu, J. Alloy. Compd. **773**, 778 (2018)
12. J Zhu, D Deng, Chem. Eng. Sci. **154**, 54 (2016)
13. Q Tian, F Zhang, L Yang, P Chen, Energy Technol. **7**, 1801048 (2019)

14. HY Mou, SX Chen, W Xiao, C Miao, R Li, GL Xu, Y Xin, SQ Nie, Ceram. Int. **47**, 19945 (2021)

15. Y Jiang, T Yuan, Y Mi, W Sun, ACS Appl. Mater. Interfaces **4**, 6216 (2012)

16. H Li, Q Su, J Kang, M Huang, M Feng, H Feng, P Huang, G Du, Mater. Lett. **217**, 276 (2018)

17. P Zhang, Y Liu, M Zhou, Y Xue, X Zeng, J Qi, M Chen, F Sun, Nanotechnology **31**, 395401 (2020)

18. AM Zhang, M Zhang, D Lan, HN Wang, YJ Tang, XL Wang, LZ Dong, L Zhang, SL Li, YQ Lan, Inorg. Chem. **57**, 11726 (2018)

19. WLIUX Huang, Z Wang, H Li, L Chen, ChemInform **42**, 156 (1998)

20. L Hong, X Huang, L Chen, J. Power Sour. **81–82**, 340 (1999)

21. C Guan, X Wang, Q Zhang, Z Fan, H Zhang, HJ Fan, Nano Lett. **14**, 4852 (2014)

22. Z Chen, Z Min, Y Cao, X Ai, H Yang, J Liu, Adv. Energy Mater. **2**, 95 (2012)

23. A Man, K Liu, Y Du, J Sun, Mater. Chem. Phys. **256**, 123669 (2020)

24. X Zhou, LJ Wan, Y-C Guo, Adv. Mater. **25**, 2152 (2013)

25. XW Guo, XP Fang, Y Sun, LY Shen, ZX Wang, LQ Chen, J. Power Sour. **226**, 75 (2013)

26. D Gao, Y Wang, Y Liu, H Sun, M Wu, H Zhang, J. Colloid Interface Sci. **538**, 116 (2019)

27. Z Wei, L Wang, M Zhuo, W Ni, H Wang, J Ma, J. Mater. Chem. A **6**, 12185 (2018)

28. B Luo, Y Hu, X Zhu, T Qiu, L Zhi, M Xiao, H Zhang, M Zou, A Cao, L Wang, J. Mater. Chem. A **6**, 1462 (2018)

29. L Pan, Y Zhang, F Lu, Y Du, Z Lu, Y Yang, T Ye, Q Liang, Y Bando, X Wang, Energy Storage Mater. **19**, 39 (2019)

30. L Ming, B Zhang, J Zhang, X Wang, H Li, C-H Wang, J. Alloy. Compd. **752**, 93 (2018)

31. Y Yang, X Zhao, H-E Wang, M Li, C Hao, M Ji, S Ren, G Cao, J. Mater. Chem. A. **6**, 3479 (2018)

32. Z Chao, Z Leiqiang, Z Ze, C Jianxin, Y Zhenyu, Y Ji, Chem. Phys. Lett. **772**, 138566 (2021)

33. Y Feng, C Bai, K Wu, H Dong, J Ke, X Huang, D Xiong, M He, J. Alloy. Compd. **843**, 156085 (2020)

34. K Ma, H Jiang, Y Hu, C Li, Adv. Funct. Mater. **28**, 1804306 (2018)

35. D Cui, Z Zheng, X Peng, T Li, T Sun, L Yuan, J. Power Sour. **362**, 20 (2017)